

An efficient Turing-type $\text{Ag}_2\text{Se-CoSe}_2$ multi-interfacial oxygen-evolving electrocatalyst

Xiao-Long Zhang

University of Science and Technology of China <https://orcid.org/0000-0002-5596-0776>

Peng-Peng Yang

University of Science and Technology of China

Ya-Rong Zheng

University of Science and Technology of China <https://orcid.org/0000-0003-2129-7774>

Yu Duan

University of Science and Technology of China

Shaojin Hu

University of Science and Technology of China

Tao Ma

University of Science and Technology of China

Fei-Yue Gao

University of Science and Technology of China

Zhuang-Zhuang Niu

University of Science and Technology of China

Zhi-Zheng Wu

University of Science and Technology of China

Shuai Qin

University of Science and Technology of China

Li-Ping Chi

University of Science and Technology of China

Xing-Xing Yu

University of Science and Technology of China

Rui Wu

University of Science and Technology of China

Chao Gu

University of Science and Technology of China

Xu-Sheng Zheng

University of Science and Technology of China

Xiao Zheng

University of Science and Technology of China <https://orcid.org/0000-0002-9804-1833>

Junfa Zhu

University of Science and Technology of China <https://orcid.org/0000-0003-0888-4261>

Min-Rui Gao (✉ mgao@ustc.edu.cn)

University of Science and Technology of China <https://orcid.org/0000-0002-7805-803X>

Article

Keywords: Ag₂Se-CoSe₂, multi-interfacial oxygen-evolving electrocatalyst

Posted Date: July 15th, 2020

DOI: <https://doi.org/10.21203/rs.3.rs-39890/v1>

License:   This work is licensed under a Creative Commons Attribution 4.0 International License.

[Read Full License](#)

Abstract

Although the Turing structures, or stationary reaction-diffusion patterns, have received increasing attention in biology and chemistry, making such unusual patterns on inorganic solids is fundamentally challenging. We report a simple cation exchange approach to produce Turing-type Ag₂Se on CoSe₂ nanobelts relied on diffusion-driven instability. The resultant Turing-type Ag₂Se-CoSe₂ material is highly effective to catalyze the oxygen evolution reaction (OER) in alkaline electrolytes with an 84.5% anodic energy efficiency. Electrochemical measurements show that the intrinsic OER activity correlates linearly with the length of Ag₂Se-CoSe₂ interfaces, determining that such Turing-type interfaces are more active sites for OER. Combining X-ray absorption and computational simulations, we ascribe the excellent OER performance to the optimized adsorption energies for critical oxygen-containing intermediates at the unconventional interfaces. Our work offers opportunities for creating Turing structures in other inorganic nanomaterials with unexplored catalytic abilities.

Introduction

Almost seven decades ago, Alan Turing predicted the chemical reaction-diffusion model, in which a pair of activator and inhibitor can interact and self-regulate to form spatiotemporal stationary patterns¹. This reaction-diffusion model has become a classic mechanism for morphogenesis in biological^{2,3} (*e.g.*, skin patterns of the pufferfish; Fig. 1a) and chemical systems⁴. In experiments on chemical systems, previous research has led to stationary Turing patterns occurred in the chlorite-iodide-malonic acid⁵⁻⁷ (CIMA) and the Belousov-Zhabotinsky^{8,9} (BZ) reactions. Later, a number of two- and three-dimensional Turing structures was investigated in chemical^{10,11} and living systems^{12,13}. Very recently, Tan and co-workers reported the preparation of a Turing-type polyamide membrane, which shows markedly enhanced water-salt separation performance compared to the conventional desalination membranes¹⁴.

Creating Turing structures in chemical systems currently remains a huge challenge. The difficulty comes from the necessary requirement that the reaction-diffusion process should evolve far from thermodynamic equilibrium^{1,15,16}, in which the inhibitors have a higher diffusion coefficient than the activators, leading to short-range activation and long-range inhibition¹⁷ (Fig. 1b). Nevertheless, in homogeneous media, most chemical reactions involve small molecules with similar or inappropriately differing diffusion coefficients^{18,19}. Such difficulty can, in principle, be overcome by introducing an unreactive reagent that reversibly binds the activator species, thus causing suitable differences in the diffusion coefficients^{6,7,14}. This has been demonstrated *via* coupling starch or polyvinyl alcohol with triiodide (activator) in the CIMA reaction⁷. Although considerable progress, there is no observation of stationary Turing patterns in inorganic solid nanomaterials has been reported thus far.

Here, we report the first experimental demonstration of Turing-type silver selenide (Ag₂Se) nanostructures that patterned on cobalt diselenide (CoSe₂) nanobelts by reacting Ag⁺ ions with previously synthesized CoSe₂ (ref. 20) in a diethylenetriamine (DETA)-deionized water (DIW) binary solution at room temperature.

The conversion from CoSe_2 to Ag_2Se is a thermodynamic driving process^{21,22}, in which the low-mobility CoSe_2 is the activator and the fast-diffusing Ag^+ ions are the inhibitor²³, thus resulting in a diffusion-driven instability and forming Turing structures. The resultant new material possesses rich Turing-type $\text{Ag}_2\text{Se-CoSe}_2$ interfaces, which manifest excellent activity for electrocatalytic oxygen evolution reaction (OER). Moreover, we show the high robustness of the Turing-type Ag_2Se nanostructures under harsh OER process. The observed OER performances can be attributed to the large number of Turing interfaces, which are experimentally and computationally confirmed as more favorable sites for the adsorption of oxygen-containing OER intermediates.

Results

Synthesis and characterization of Turing-type $\text{Ag}_2\text{Se-CoSe}_2$

Stationary Turing patterns have been widely observed in living systems^{12,13,15}, such as *diodon holocanthus* (commonly known as the pufferfish; Fig. 1 a). The striped patterns in the pufferfish inspired that a high density of interfaces are likely created when Turing structure can be made in inorganic materials. Chemical transformation of one inorganic solid to another by atom exchange in solution is generally considered as a reaction-diffusion process²⁴. This transformation, also known as ion-exchange reaction, has previously been used to pattern solids on nanoscale, leading to new materials with higher compositional and structural complexity²⁵. We hypothesize here that cation exchange may offer the ability to generate a Turing pattern once the diffusion coefficients of two cations are appropriately different.

We want to react CoSe_2 nanobelts with Ag^+ ions to produce Ag_2Se , considering that the conversion to Ag_2Se is thermodynamically favored with a driving force of around $-1000 \text{ kJ mol}^{-1}$ in the bulk²⁶. The previously developed CoSe_2 nanobelts²⁰ (Supplementary Fig. 1) are the material of choice because they can provide adequate surface regions for the development of Turing structures. In a typical synthesis, the as-synthesized CoSe_2 nanobelts were dispersed in a mixture of DETA and DIW (2/1, v/v) under vigorous stirring. After completely dispersing, AgNO_3 was added and the reaction solution was continuously stirred at room temperature for 4 hours. In this system, CoSe_2 is the activator, and AgNO_3 is the inhibitor (Fig. 1b). The reaction starts when the fast-diffusing Ag^+ comes to the CoSe_2 surface and replaces Co^{2+} ions in the solid phase. Because the markedly lower diffusion of Co^{2+} , this activator initially replaced by the locally available Ag^+ inhibitor. As the reaction proceeds, more Co^{2+} activator diffuses to exchange with nearby inhibitor, and eventually a Turing-type Ag_2Se pattern forms across the surface of the CoSe_2 nanobelts (Fig. 1c). We note that the diffusion coefficient of Ag^+ ions is $\sim 10^{-5} \text{ cm}^2 \text{ s}^{-1}$ (ref. 23), orders of magnitude higher than that of Co^{2+} ions in CoSe_2 . Such differences in the diffusion coefficients of the two species thus meet the requirement of activator/inhibitor-mediated patterning, which result in the unusual Turing structures (Fig. 1c).

We examined the surface morphology of the as-synthesized sample by scanning electron microscopy (SEM), which shows regular striped patterns over the entire CoSe_2 support (Fig. 2a, Supplementary Fig. 2). Transmission electron microscopy (TEM; Fig. 2b) and scanning TEM (STEM; Fig. 2c) studies reveal that very refined and interconnected Ag_2Se networks grew on CoSe_2 , forming the nanoscale Turing-type structures. To visualize the Ag_2Se - CoSe_2 interfacial structure, we performed high-angle annular dark-field STEM (HAADF-STEM). Figure 2d validates the formation of distinct solid-state interface with the contrast mainly from the difference in atomic number between Ag_2Se and CoSe_2 (Supplementary Fig. 3). The dashed circles in Figure 2d highlight different lattice configurations, and their corresponding fast Fourier transform (FFT) patterns feature cubic CoSe_2 (Fig. 2e) and orthorhombic Ag_2Se (Fig. 2f), respectively. Energy-dispersive X-ray spectrum (EDX) elemental mappings further evidence that Ag_2Se developed on the CoSe_2 support, where Ag appears only in the Turing-patterned regions (Supplementary Figs. 4, 5). Additionally, our X-ray diffraction (XRD; Supplementary Fig. 6a) measurements confirm the combination of cubic CoSe_2 (JCPDS 09-0234) and orthorhombic Ag_2Se (JCPDS 24-1041) phases, consistent with the Raman results (Supplementary Fig. 6b).

We carried out a series of control experiments to explore the formation of Turing-type Ag_2Se - CoSe_2 structure. Despite cation exchange is commonly prohibited at room temperature in the bulk phase, results show that our reaction happened at room temperature with a fast rate. This phenomenon could be ascribed to the reduced reaction barrier in nanosized materials²⁷, as well as the favorable thermodynamic driving force for forming Ag_2Se (ref. 26). We tracked the evolution of the Turing structures as a function of reaction time (Supplementary Figs. 7, 8). The diffusion-driven instability allowed this Turing structures to develop well at mere 1 h; markedly prolonging the reaction time to 12 h resulted in a hollowed-out structure. Moreover, the concentration of AgNO_3 appears to be also critical (Supplementary Figs. 9-11). At low Ag^+ concentration, the transformation reaction initiated only at the edges of CoSe_2 nanobelts where the Co^{2+} diffusion is easier because of the energy minimization. The addition of excess Ag^+ would cause the formation of over-carved material. Our experiments thus reveal that reacting 7.84 mmol L^{-1} AgNO_3 with CoSe_2 at room temperature for 4 h yields the optimal Turing-type Ag_2Se - CoSe_2 structure.

We investigated the physicochemical properties of the novel Turing-type Ag_2Se - CoSe_2 material by multiple characterization techniques. Differential scanning calorimetry (DSC) in Figure 2g exhibits a pair of endothermic (located at 417 K) and exothermal (located at 360 K) peaks for the Ag_2Se - CoSe_2 , which could be the result of a phase transition from low-temperature cubic to high-temperature superionic phase of Ag_2Se (ref. 28) (Insets in Fig. 2g). This superionic conducting phase transition of Ag_2Se - CoSe_2 thus hints at potentially high cation mobility of the new structure²⁹. Electrical conductivity tests as a function of temperature reveal consistently higher conductivity of the Ag_2Se - CoSe_2 than that of metallic CoSe_2 (Fig. 2h). Such conductivity enhancement suggests that the Turing-type Ag_2Se - CoSe_2 interfaces facilitate electron transfer. Moreover, we performed the work function measurement of Ag_2Se , CoSe_2 , and Ag_2Se - CoSe_2 by ultraviolet photoelectron spectroscopy (UPS; Fig. 2i). The results show a lower work

function of 3.73 eV for $\text{Ag}_2\text{Se-CoSe}_2$, versus 3.93 eV for CoSe_2 and 4.24 eV for Ag_2Se , indicating a modulated electronic structure of $\text{Ag}_2\text{Se-CoSe}_2$ that permit an easier electron transfer, in line with conductivity results³⁰.

OER performance of Turing-type $\text{Ag}_2\text{Se-CoSe}_2$ catalyst

The boosted electron transfer property of $\text{Ag}_2\text{Se-CoSe}_2$ prompted us to explore this new structure for negotiating the sluggish OER catalysis, considering that decent OER activities have been observed previously on CoSe_2 -based catalysts³¹⁻³⁴. We compared the OER activity of our Turing-type $\text{Ag}_2\text{Se-CoSe}_2$ catalyst with that of four references CoSe_2 , Ag_2Se , NiFe LDH, and 20 wt% Ir/C catalysts. Rotating disk electrode (RDE) measurements in O_2 -saturated 0.1 M KOH exhibit that $\text{Ag}_2\text{Se-CoSe}_2$ needs an overpotential of mere 221 mV at 10 mA cm^{-2} , which increased to 399 mV for CoSe_2 , 350 mV for NiFe LDH, and 393 mV for Ir/C (Fig. 3a). By sharp contrast, Ag_2Se itself affects negligible OER activity. Tafel analysis (Fig. 3b) yields a slope of 52, 175, 66 and 101 mV decade^{-1} for $\text{Ag}_2\text{Se-CoSe}_2$, CoSe_2 , NiFe LDH and Ir/C catalyst, respectively. A considerably smaller slope achieved in $\text{Ag}_2\text{Se-CoSe}_2$ implies markedly enhanced kinetics for OER. We also conducted electrochemical impedance spectroscopy (EIS) at 340 mV overpotential to probe the charge transfer resistance (R_{ct}) for these catalysts. Our measurements (Supplementary Fig. 12) exhibit that the R_{ct} of $\text{Ag}_2\text{Se-CoSe}_2$ is ~ 13 ohms, versus ~ 41 , 18573, 30, 148 ohms for CoSe_2 , Ag_2Se , NiFe LDH and Ir/C catalyst, respectively. The smaller R_{ct} for $\text{Ag}_2\text{Se-CoSe}_2$ suggests an improved charge transfer between the catalyst surface and sorbates (*e.g.*, O_2^{2-} and O^{2-}) in the OER process³⁵. This result agrees well with our double-layer capacitance (C_{dl}) measurements (Supplementary Figs. 13) that give the largest C_{dl} value for $\text{Ag}_2\text{Se-CoSe}_2$, which also matches with our conductivity and work function results that $\text{Ag}_2\text{Se-CoSe}_2$ allows more favorable electron transfer.

We systematically assessed the OER performances of the $\text{Ag}_2\text{Se-CoSe}_2$ catalysts that synthesized at different reaction times and Ag^+ concentrations, results of which we show in Supplementary Figures 14 to 16. We uncovered that $\text{Ag}_2\text{Se-CoSe}_2$ with unique Turing-type structure gives the optimal catalytic property, so the rich Turing interfaces aforementioned could be responsible for the superior OER activity. We also underscore that the performance gained from the RDE testing here ranks among the superb for the OER electrocatalysts reported previously (Supplementary Fig. 17). Besides activity, the $\text{Ag}_2\text{Se-CoSe}_2$ catalyst also exhibits excellent operating stability (Supplementary Figs. 18 and 19). For example, our multistep chronopotentiometry recorded at 10, 30 and 50 mA cm^{-2} reveals mere a small decay over 70 h of continuous electrolysis (Supplementary Fig. 19).

To verify the hypothesis that Turing-type $\text{Ag}_2\text{Se-CoSe}_2$ interfaces are more OER active sites, we plotted the exchange current density (j_0 ; the most inherent measure of OER activity^{36,37}) of each sample versus the Ag_2Se interface length and the Ag_2Se covered area (Figs. 3c and d, Supplementary Figs. 20-22), respectively. We find that the j_0 increases linearly as the interface length is increased (Fig. 3c). When

plotting versus the Ag₂Se covered area, a volcano-shaped dependence of the j_0 was obtained (Fig. 3d), further revealing that the reaction rate is directly proportional to the amount of interface sites. These results thus elucidate that the OER reaction takes place more energetically at the Ag₂Se-CoSe₂ interfaces.

We used gas chromatography (GC) to detect and quantify the O₂ product evolved from the Ag₂Se-CoSe₂-decorated carbon paper electrode at 10 mA cm⁻². The measured O₂ gas perfectly matches with the theoretical value, corresponding to a Faradaic efficiency of ~100% (Fig. 3e). As a result, we achieved a high anodic energy efficiency up to 84.5%, which far exceeds that of CoSe₂ (73.7%) and also compares favorably to 76.2% for NiFe LDH and 74.4% for Ir/C catalyst (Fig. 3f), respectively.

Spectroscopic studies of the Turing-type Ag₂Se-CoSe₂ catalyst

We now study the impact of Ag₂Se-CoSe₂ interfaces on the electronic structure and catalytic character by using diverse spectroscopic techniques. Prior reports have demonstrated that orthorhombic Ag₂Se contains Ag (1) occurring in tetrahedral coordination and Ag (2) in triangular coordination³⁸ (Supplementary Fig. 23). Our valence band spectrum of Ag₂Se reveals two intensive features at 5.31 and 6.15 eV (Fig. 4a), originating from Ag (1) 5*d* and Ag (2) 5*d* states³⁹, respectively. When forming interfaces with CoSe₂, a large negative shift (~190 mV) of the Ag (1) 5*d* state is observed, whereas the Ag (2) 5*d* feature is undisturbed. This result suggests that Ag⁺ coordinates tetrahedrally with Se²⁻ at the novel Turing-type interfaces (Supplementary Fig. 24).

Figure 4b presents the Co K-edge X-ray absorption near-edge structure (XANES), which shows that the absorption edge of Ag₂Se-CoSe₂ is shifted to a lower energy versus CoSe₂ because of charge transfer from Ag₂Se to Co (Supplementary Fig. 25)⁴⁰. Extended X-ray absorption fine structure (EXAFS) spectra (Fig. 4c) of Ag₂Se-CoSe₂ and CoSe₂ are similar, both showing a peak at ~2.04 Å that ascribed to Co-Se (ref. 33). After OER, two distinct peaks appear in EXAFS spectra: the former at 1.47 Å is due to Co-O, and the latter 2.40 Å is attributed to Co-Co, indicating the formation of CoOOH because of surface self-reconstruction of Ag₂Se-CoSe₂ catalyst during OER (ref. 41). Intriguingly, the peak at 2.04 Å, characteristic of CoSe₂, is still observed after OER (Fig. 4c). By contrast, single CoSe₂ undergoes a complete surface self-reconstruction to form CoOOH after OER (Supplementary Fig. 26). The EXAFS wavelet transform (Fig. 4d) analyses—a technique that can discriminate the backscattering atoms—further verify that Co-Se bond (~ 7.82 Å⁻¹ in *k* space) remains in Ag₂Se-CoSe₂ after OER.

Unexpectedly, our Ag 3*d* X-ray photoelectron spectroscopy (XPS) analysis (Fig. 4e) reveals that the Ag valence state is unaltered after we performed OER on Ag₂Se-CoSe₂ catalyst at a 221 mV overpotential (10 mA cm⁻²) for 12 h. Moreover, the signal from Ag-Se bond (at 54.2 eV)⁴² in Se 3*d* (Fig. 4f, Supplementary Fig. 27) further supports that Ag₂Se phase survives after OER, agreeing with Se K-edge XANES results (Fig. 4g, Supplementary Fig. 28). By contrast, only oxidized Se species⁴³ were detected from single CoSe₂ catalyst after OER (Fig. 4f), suggesting a complete surface self-reconstruction to CoOOH.

On the basis of above results, we become clear about the nature at the Turing-type $\text{Ag}_2\text{Se-CoSe}_2$ interfaces. In the reaction-diffusion system, Ag^+ ions replace the Co^{2+} ions in CoSe_2 nanobelts and tetrahedrally coordinates with Se^{2-} , creating Turing-type $\text{Ag}_2\text{Se-CoSe}_2$ interfaces where the e_g filling of adjacent Co cations is increased. This hence causes a near-unity e_g occupancy of surface Co cations, leading to enhanced OER activity^{40,44}. Moreover, such interfaces also show extreme structural robustness against harsh OER corrosion (Fig. 4h).

Density functional theory calculations

To better understand the catalytic nature of the $\text{Ag}_2\text{Se-CoSe}_2$ interfaces, we carried out density functional theory (DFT) calculations. On the basis of experimental characterizations above, we created the $\text{Ag}_2\text{Se-CoSe}_2$ model by bridging Ag_2Se (112) and CoSe_2 (210) surfaces; regions remote to the interface were replaced with CoOOH to represent the catalyst during OER (Supplementary Figs. 29, 30). Detailed reaction-pathway calculations (Fig. 5a) reveal that the desorption of $^*\text{OOH}$ to generate O_2 on CoSe_2 (210) is kinetically hindered because of the high barrier of 2.976 eV. On the interface sites, the rate-determining $^*\text{OOH}$ intermediate is reduced by 0.904 eV, which gives a weaker $^*\text{OOH}$ adsorption, consistent with our Bader charge analysis⁴⁵ (Supplementary Fig. 31). DFT calculations further predict that the Co-O bond length increases from 1.79 to 1.84 Å on the $\text{Ag}_2\text{Se-CoSe}_2$ interface (Supplementary Fig. 32), which explains the weaker $^*\text{OOH}$ adsorption on $\text{Ag}_2\text{Se-CoSe}_2$ interface relative to CoSe_2 .

A plot of the electron density difference (Fig. 5b) displays that the donation of electrons from the Ag_2Se to nearby Co sites occurs at the interface, which permits e_g -orbital occupancy of Co closer to unity and thus enhanced OER activity^{40,44}, matching well with our XANES measurements. Moreover, the calculated projected density of states (PDOS; Fig. 5c) shows that the d -band center of Co atom in $\text{Ag}_2\text{Se-CoSe}_2$ deviates more from the Fermi level than that of single CoSe_2 (210), further evidencing the weak binding of $^*\text{OOH}$ intermediate on the $\text{Ag}_2\text{Se-CoSe}_2$ interfaces⁴⁶.

Lastly, to examine the O_2 binding abilities of $\text{Ag}_2\text{Se-CoSe}_2$ and CoSe_2 catalysts, we performed the temperature-programmed desorption analysis. Figure 5d shows that $\text{Ag}_2\text{Se-CoSe}_2$ gives a lower O_2 onset desorption temperature of 111 °C versus single CoSe_2 (195 °C), which we consider to benefit the rate-determining $^*\text{OOH}$ desorption step for improved O_2 release. Thus, our results, both experimentally and computationally, have demonstrated that the Turing-type $\text{Ag}_2\text{Se-CoSe}_2$ interfaces are more energetically favored to catalyze the OER.

Conclusion

Chemical Turing patterns in inorganic nanomaterials have not yet been reported. Here we demonstrate that Turing-driven morphogenesis occurs in a cation exchange process, which was originated from the appropriate differences between the diffusion coefficients of Ag^+ and Co^{2+} (diffused from CoSe_2),

creating stationary Ag_2Se Turing patterns on CoSe_2 nanobelts. The obtained new material comprises abundant Turing-structured $\text{Ag}_2\text{Se-CoSe}_2$ interfaces, which enable excellent OER electrocatalytic activity and stability in alkaline electrolyte. Our work opens the possibility of producing stationary reaction-diffusion patterns in inorganic solids that would not otherwise have such structures. Furthermore, the unusual engineered interfaces may see application in a wider spectrum of electrocatalytic processes.

Methods

Material synthesis

All chemicals are of analytical grade and were used as received without further purification.

Synthesis of $\text{CoSe}_2/\text{DETA}$ nanobelts

The $\text{CoSe}_2/\text{DETA}$ nanobelts were synthesized by a hydrothermal method using our previously developed method²⁰. Briefly, 0.249 g $\text{Co}(\text{AC})_2 \cdot \text{H}_2\text{O}$ and 0.173 g Na_2SeO_3 were added into a mixed solution (40 ml) with a volume ratio of $V_{\text{DETA}}/V_{\text{DIW}} = 2:1$ (DIW = deionized water). After stirring for 30 min, the obtained wine solution was transferred into a Teflon-lined autoclave, which was sealed and maintained at 180 °C for 17 h. The resulting CoSe_2 nanobelts were carefully washed and dried before use.

Synthesis of Turing-type $\text{Ag}_2\text{Se-CoSe}_2$ catalyst

The Turing-type $\text{Ag}_2\text{Se-CoSe}_2$ was prepared through an ion-exchange reaction. Briefly, 20 mg freshly made CoSe_2 nanobelts was added into a mixed solution (15 mL) with a volume ratio of $V_{\text{DETA}}/V_{\text{DIW}} = 2:1$. After completely dispersing, 20 mg AgNO_3 was added and drastically stirring at room temperature for 4 h, the obtained Turing-type $\text{Ag}_2\text{Se-CoSe}_2$ powder was carefully washed and dried before use.

Material characterizations

X-ray powder diffraction (XRD) was obtained from a Philips X'Pert Pro Super X-ray diffractometer with $\text{Cu K}\alpha$ radiation ($\lambda = 1.54178 \text{ \AA}$). The morphology of the samples was achieved by SEM (Zeross Supra 40) and TEM (Hitachi H7650). The STEM and HAADF images, SAED, and EDX elemental mappings were measured on JEMARM 200F Atomic Resolution Analytical Microscope with an acceleration voltage of 200 kV. Raman spectra were taken on a Raman microscope (Renishaw®) excited with a 514 nm excitation laser. ICP-AES data were investigated by an Optima 7300 DV instrument. Ultraviolet-photoelectron spectroscopy was obtained at the BL11U beamline of National Synchrotron Radiation Laboratory in Hefei, China. The X-ray absorption spectra of Co L-edges were taken on the BL10B beamline of National Synchrotron Radiation Laboratory in Hefei (China). The X-ray absorption spectra of Co and Se K-edges were carried out at the beamline 14W1 of Shanghai synchrotron Radiation Laboratory (China). XPS was performed on an X-ray photoelectron spectrometer (ESCALab MKII) with an X-ray source ($\text{Mg K}\alpha$ $h\nu=1253.6 \text{ eV}$). The O_2 - temperature-programmed desorption analysis (TPD)

measurements were taken on AutoChem II 2920. The electrical conductivity measurements were measured by using the standard four probe transport measurement on commercial apparatus of Physical Property Measurement System (Quantum Design, PPMS). Differential scanning calorimetry (DSC) cycling curves were carried out by the NETZSCH DSC Q2000 with a heating/cooling rate of 5 K min^{-1} between 273 and 473 K.

Electrochemical measurements

All the electrochemical measurements were performed in a standard three-electrode cell at ambient temperature connected to a VSP-300 potentiostat (BioLogic, France). Ag/AgCl (3.5 M KCl) electrode and graphite rod were used as the reference and counter electrodes, respectively. The potentials reported in this work were normalized versus the RHE through a standard RHE calibration ($E = E_{\text{Ag/AgCl}} + 0.97 \text{ V}$). A rotating disk electrode (RDE) with glassy carbon (PINE, 5.00 mm diameter, disk area: 0.196 cm^2) was used as the working electrode.

To make the working electrodes, 5 mg catalyst powder was dispersed in 1 ml of 1:3 v/v isopropanol/DIW mixture with 20 μL Nafion solution (5 wt%), which was ultrasonicated to yield a homogeneous ink. Then, 8 μL catalyst ink was pipetted onto the glassy carbon disk to ensure the catalyst loading of $\sim 0.2 \text{ mg cm}^{-2}$. The fresh electrolytes (0.1 M KOH) were bubbled with pure oxygen for 30 min before measurements. The electrodes were pre-cycled between 0 and 0.8 V vs. Ag/AgCl at a sweep rate of 100 mV s^{-1} for 30 cycles until reaching the stable state, then the OER polarization curves were recorded at a sweep rate of 2 mV s^{-1} and 1600 r.p.m (to remove the O_2 bubbles formed *in situ*) at ambient temperature. The EIS measurement was performed in the same configuration at 340 mV overpotential over a frequency range from 100 KHz to 100 mHz at the amplitude of the sinusoidal voltage of 5 mV. The polarization curves were re-plotted as overpotential (η) versus log current ($\log j$) to get Tafel plots to assess the HER kinetics of investigated catalysts. The Tafel slope (b) can be obtained by fitting the linear portion of the Tafel plots to the Tafel equation ($\eta = a + b \log j$). The exchange current density (j_0) were calculated from Tafel curves using extrapolation method. The values of mass activity (A mg^{-1}) were calculated from the catalyst loading m (0.2 mg cm^{-2}) and the current density of 10 mA cm^{-2} : mass activity = j / m .

The $\text{Ag}_2\text{Se-CoSe}_2$ -modified carbon paper (catalyst loading: $\sim 0.20 \text{ mg cm}^{-2}$) was used as working electrode to conduct chronopotentiometry experiments. The O_2 product, evolved from the $\text{Ag}_2\text{Se-CoSe}_2$ -decorated carbon paper electrode at 10 mA cm^{-2} , was detected and quantified by gas chromatography. The accelerated stability measurements were carried out by potential cycling between 0 and 0.6 V Ag/AgCl at a sweep rate of 100 mV s^{-1} . After cycling, the resultant electrode was used for polarization curves with a sweep rate of 2 mV s^{-1} . To estimate the double-layer capacitance, cyclic voltammograms were measured at different sweep rates in the potential region of 1.25-1.35 versus RHE at ambient temperature. All the polarization curves were corrected with iR compensation that resulted from the solution resistance.

Anodic energy efficiency calculations

Anodic energy efficiency was calculated via the following formula⁴⁷: (see Formula 1 in the Supplementary Files)

where E^0 is the equilibrium cell potential for water decomposition ($E^0 = 1.23$ V). FE is the Faradaic efficiency for H_2O to O_2 conversion, and η_{an} is the overpotential at the anode and was measured at 10 mA cm^{-2} in this work.

DFT calculations

The overall OER process includes four elementary steps that follow: (see Reactions 1-4 in the Supplemental Files)

Here, (*) denotes the $-OH$ terminated $CoSe_2$ or $Ag_2Se-CoSe_2$ surface. We used $-OH$ groups to replace the unsaturated Se atoms as models to represent the surface hydroxylation of $CoSe_2$ or $Ag_2Se-CoSe_2$, because the whole structure is well maintained. These are similar to the $-OH$ groups terminated surface of oxide models⁴⁸. It is more convenient to calculate the thermochemistry of the OER under acidic condition. Following Bajdich *et al.*⁴⁹, we consider the following elementary steps: (see Reactions 5-8 in the Supplemental Files)

Reactions 5-8 are thermodynamically equivalent to reactions 1-4 shown above.

The Gibbs free energy changes are calculated as follows: (see Changes in the Supplemental Files)

The G values are calculated by: (see Formula 2 in the Supplemental Files)

E_{DFT} is the total energy from the DFT calculation. E_{ZPE} is the zero-point energy, S is the entropy and T is the temperature (298K). The energy of is got from the energy of using the standard hydrogen electrode (SHE). The bond energy is calculated by: (see Formula 3 in the Supplemental Files)

The density functional theory calculations were performed by Vienna ab initio simulation package (VASP)⁵⁰ program with projector augmented wave (PAW) method and the kinetic energy cut off was set to be 500 eV. The convergence criterion for the electronic self-consistent iteration was set to be 10^{-4} eV. The atomic positions were fully relaxed until the force on each atom is less than 0.02 eV \AA^{-1} . The Perdew-Burke-Ernzerhof (PBE)⁵¹ generalized gradient approximation (GGA) exchange-correlation functional was used throughout. The slab model of $CoSe_2$ (210) surface was constructed based on the optimized crystal structure and we selected the right Ag_2Se cluster anchored on the $CoSe_2$ (210) surface. The vacuum layer was set to be 15 \AA to ensure the separation between slabs.

Declarations

Acknowledgements:

This work was supported by the funding support from the National Natural Science Foundation of China (Grants 21975237 and 51702312), the National Basic Research Program of China (Grant 2018YFA0702001), the Fundamental Research Funds for the Central Universities (WK2340000076), and the Recruitment Program of Global Youth Experts. This work was partially performed at the USTC Center for Micro and Nanoscale Research and Fabrication.

Author Contributions:

M.-R.G. conceived and supervised the project. X.-L.Z. and P.-P.Y. performed the experiments, collected and analyzed the data. X.-S.Z. and J.-F.Z. performed XPS and UPS measurements. X.-L.Z., S.-J.H and X.Z. carried out the DFT calculations. T.M., F.-Y.G., Z.-Z.W., Z.-Z.N., Y.-R.Z., X.-X.Y., R.W., Y.D., C.G., L.-P.C. and S.Q. helped with electrochemical data collection and analysis. M.-R.G. and X.-L.Z. co-wrote the manuscript. All authors discussed the results and commented on the manuscript.

Additional information:

Supplementary information is available in the online version of the paper. Correspondence and requests for materials should be addressed to M.R.G.

Competing financial interests:

The authors declare no competing financial interests.

References

- 1 Turing, A. M. The chemical basis of morphogenesis. *Phil. Trans. R. Soc. Lond. B* **237**, 37-72 (1952).
- 2 Meinhardt, H. *Models of biological pattern formation*. (Academic Press, 1982).
- 3 Murray, J. D. *Mathematical biology*. (Springer, 1989).
- 4 Nicolis, G. & Prigogine, I. *Self-Organization in Nonequilibrium Systems*. (Wiley, 1977).
- 5 De Kepper, P., Epstein, I. R., Kustin, K. & Orban, M. Batch oscillations and spatial wave patterns in chlorite oscillating systems. *J. Phys. Chem.* **86**, 170-171 (1982).
- 6 Castets, V. V., Dulos, E., Boissonade, J. & De Kepper, P. Experimental evidence of a sustained standing Turing-type nonequilibrium chemical pattern. *Phys. Rev. Lett.* **64**, 2953-2956 (1990).
- 7 Ouyang, Q. & Swinney, H. L. Transition from a uniform state to hexagonal and striped Turing patterns. *Nature* **352**, 610-612 (1991).

- 8 Vanag, V. K. & Epstein, I. R. Pattern formation in a tunable medium: the Belousov-Zhabotinsky reaction in an aerosol OT microemulsion. *Phys. Rev. Lett.* **87**, 228301 (2001).
- 9 Epstein, I. R. & Xu, B. Reaction-diffusion processes at the nano- and microscales. *Nat. Nanotech.* **11**, 312-319 (2016).
- 10 Jr., T. B., Vanag, V. K. & Epstein, I. R. Tomography of Reaction-Diffusion Microemulsions Reveals Three-Dimensional Turing Patterns. *Science* **331** (2011).
- 11 Liu, T., Dou, X., Xu, Y., Chen, Y. & Han, Y. In Situ Investigation of Dynamic Silver Crystallization Driven by Chemical Reaction and Diffusion. *Research* **2020**, 4370817 (2020).
- 12 Sick, S., Reinker, S., Timmer, J. & Schlake, T. WNT and DKK Determine Hair Follicle Spacing Through a Reaction-Diffusion Mechanism. *Science* **314**, 1447–1450 (2006).
- 13 Economou, A. D. *et al.* Periodic stripe formation by a Turing mechanism operating at growth zones in the mammalian palate. *Nat. Genet.* **44**, 348 (2012).
- 14 Tan, Z., Chen, S., Peng, X., Lin Zhang & Gao, C. Polyamide membranes with nanoscale Turing structures for water purification. *Science* **360**, 518–521 (2018).
- 15 Kondo, S. & Miura, T. Reaction-diffusion model as a framework for understanding biological pattern formation. *Science* **329**, 1616-1620 (2010).
- 16 Horváth, J., Szalai, I. & Kepper, P. D. An Experimental Design Method Leading to Chemical Turing Patterns. *Science* **324**, 772-775 (2009).
- 17 Gierer, A. & Meinhardt, H. A Theory of Biological Pattern Formation. *Kybernetik* **12**, 30–39 (1972).
- 18 Iida, Y., Yamaguchi, T. & Tanaka, T. Experimental and Modeling Study on Diffusion of Selenium under Variable Bentonite Content and Porewater Salinity. *J. Nucl. Sci. Technol.* **48**, 1170-1183 (2011).
- 19 Harned, H. S. The Diffusion Coefficients of the Alkali Metal Chlorides and Potassium and Silver Nitrates in Dilute Aqueous Solutions at 25°. *Proc. Natl. Acad. Sci. USA* **40**, 551 (1954).
- 20 Gao, M.-R., Yao, W.-T., Yao, H.-B. & Yu, S.-H. Synthesis of Unique Ultrathin Lamellar Mesostuctured CoSe₂-Amine (Protonated) Nanobelts in a Binary Solution. *J. Am. Chem. Soc.* **131**, 7486-7487 (2009).
- 21 De Trizio, L. & Manna, L. Forging colloidal nanostructures via cation exchange reactions. *Chem. Rev.* **116**, 10852-10887 (2016).
- 22 Zhang, D. *et al.* Phase-selective cation-exchange chemistry in sulfide nanowire systems. *J. Am. Chem. Soc.* **136**, 17430-17433 (2014).

- 23 Firth, J. & Tyrrell, H. Diffusion coefficients for aqueous silver nitrate solutions at 25°, 35°, and 45° from diaphragm-cell measurements. *J. Chem. Soc.*, 2042-2047 (1962).
- 24 Moon, G. D. *et al.* Chemical transformations of nanostructured materials. *Nano Today* **6**, 186-203 (2011).
- 25 Robinson, R. D. *et al.* Spontaneous superlattice formation in nanorods through partial cation exchange. *Science* **317**, 355-358 (2007).
- 26 Burgess, J. *Metal ions in solution*. (Ellis Horwood, Sussex, UK, 1978).
- 27 Son, D. H., Hughes, S. M., Yin, Y. & Alivisatos, A. P. Cation exchange reactions in ionic nanocrystals. *Science* **306**, 1009-1012 (2004).
- 28 Wang, J. *et al.* Tetragonal–Orthorhombic–Cubic Phase Transitions in Ag₂Se Nanocrystals. *Chem. Mater.* **26**, 5647-5653 (2014).
- 29 Boolchand, P. & Bresser, W. Mobile silver ions and glass formation in solid electrolytes. *Nature* **410**, 1070-1073 (2001).
- 30 Bard, A. J. & Faulkner, L. R. *Electrochemical methods: fundamentals and applications*. (Wiley, 2001).
- 31 Gao, M.-R. *et al.* Nitrogen-Doped Graphene Supported CoSe₂ Nanobelt Composite Catalyst for Efficient Water Oxidation. *Acs Nano* **8**, 3970–3978 (2014).
- 32 Gao, M. R., Xu, Y. F., Jiang, J., Zheng, Y. R. & Yu, S. H. Water oxidation electrocatalyzed by an efficient Mn₃O₄/CoSe₂ nanocomposite. *J. Am. Chem. Soc.* **134**, 2930-2933 (2012).
- 33 Liu, Y. *et al.* Low overpotential in vacancy-rich ultrathin CoSe₂ nanosheets for water oxidation. *J. Am. Chem. Soc.* **136**, 15670-15675 (2014).
- 34 Dou, Y. *et al.* Approaching the activity limit of CoSe₂ for oxygen evolution via Fe doping and Co vacancy. *Nat. Commun.* **11**, 1664 (2020).
- 35 Niu, L., Li, Q., Wei, F., Chen, X. & Wang, H. Electrochemical impedance and morphological characterization of platinum-modified polyaniline film electrodes and their electrocatalytic activity for methanol oxidation. *J. Electroanal. Chem.* **544**, 121-128 (2003).
- 36 Oh, H. S. *et al.* Electrochemical Catalyst-Support Effects and Their Stabilizing Role for IrOx Nanoparticle Catalysts during the Oxygen Evolution Reaction. *J. Am. Chem. Soc.* **138**, 12552-12563 (2016).

- 37 Huynh, M., Bediako, D. K. & Nocera, D. G. A Functionally Stable Manganese Oxide Oxygen Evolution Catalyst in Acid. *J. Am. Chem. Soc.* **136**, 6002-6010 (2014).
- 38 Billetter, H. & Ruschewitz, U. Structural phase transitions in Ag₂Se (naumannite). *Z. Anorg. Allg. Chem.* **634**, 241-246 (2008).
- 39 Kashida, S. *et al.* Electronic structure of Ag₂S, band calculation and photoelectron spectroscopy. *Solid State Ionics* **158**, 167-175 (2003).
- 40 Suntivich, J., May, K. J., Gasteiger, H. A., Goodenough, J. B. & Shao-Horn, Y. A perovskite oxide optimized for oxygen evolution catalysis from molecular orbital principles. *Science* **334**, 1383-1385 (2011).
- 41 Song, S. *et al.* Operando X-ray spectroscopic tracking of self-reconstruction for anchored nanoparticles as high-performance electrocatalysts towards oxygen evolution. *Energy Environ. Sci.* **11**, 2945-2953 (2018).
- 42 Khanna, P., Singh, N., Charan, S. & Patil, K. Synthesis of β-Ag₂Se from organo-selenium precursor and silver nitrate in DMF via simultaneous reduction of selenium and silver salt. *Mater. Lett.* **60**, 2080-2085 (2006).
- 43 Rupp, H. & Weser, U. X-ray photoelectron spectroscopy of some selenium containing amino acids. *Bioinorg. Chem.* **5**, 21-32 (1975).
- 44 Li, X. *et al.* Enhancing oxygen evolution efficiency of multiferroic oxides by spintronic and ferroelectric polarization regulation. *Nat. Commun.* **10** (2019).
- 45 Liu, M. *et al.* Enhanced electrocatalytic CO₂ reduction via field-induced reagent concentration. *Nature* **537**, 382-386 (2016).
- 46 Cai, J. *et al.* N-induced lattice contraction generally boosts the hydrogen evolution catalysis of P-rich metal phosphides. *Sci. Adv.* **6**, eaaw8113 (2020).
- 47 Arquer, F. P. G. d. *et al.* CO₂ electrolysis to multicarbon products at activities greater than 1 A cm⁻². *Science* (2020).
- 48 Liao, P., Keith, J. A. & Carter, E. A. Water oxidation on pure and doped hematite (0001) surfaces: Prediction of Co and Ni as effective dopants for electrocatalysis. *J. Am. Chem. Soc.* **134**, 13296-13309 (2012).
- 49 Bajdich, M., García-Mota, M., Vojvodic, A., Nørskov, J. K. & Bell, A. T. Theoretical investigation of the activity of cobalt oxides for the electrochemical oxidation of water. *J. Am. Chem. Soc.* **135**, 13521-13530 (2013).

50 Kresse, G. & Furthmüller, J. Efficient iterative schemes for ab initio total-energy calculations using a plane-wave basis set. *Phys. Rev. B* **54**, 11169 (1996).

51 Perdew, J. P., Burke, K. & Ernzerhof, M. Generalized gradient approximation made simple. *Phys. Rev. Lett.* **77**, 3865 (1996).

Figures

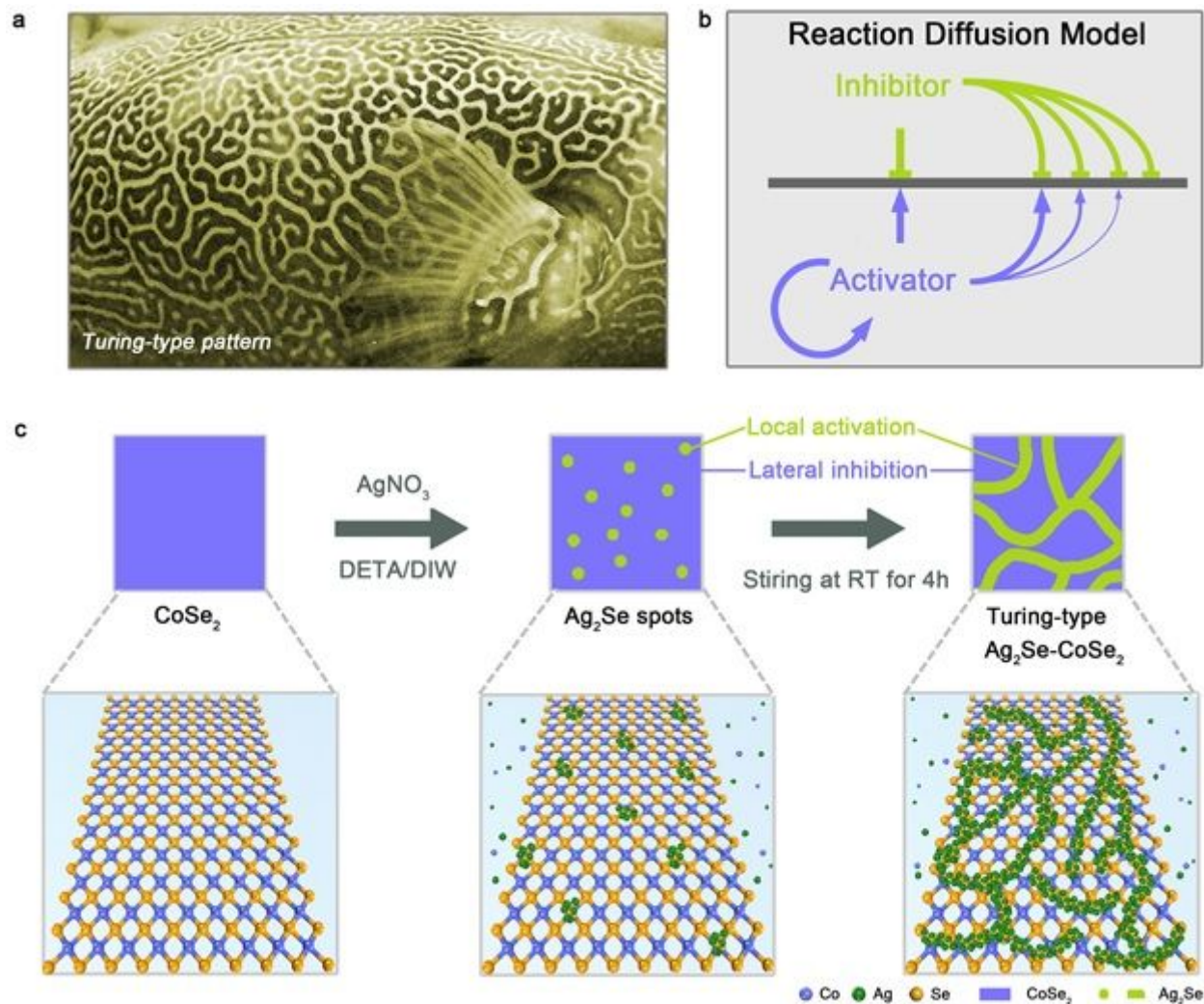


Figure 1

Formation of Turing-type structures. a, Photograph of the skin of a pufferfish, showing stationary Turing patterns. b, Schematic diagram of activator-inhibitor interaction in a reaction-diffusion process. Reactions leading to Turing-type structures depend on competing activation (purple) and inhibition (green) kinetic pathways. c, Schematic illustration of the formation of inorganic Turing system via ion-exchange reaction. In this system, CoSe₂ is the activator, and AgNO₃ is the inhibitor. The different diffusion coefficients between Co²⁺ in CoSe₂ and Ag⁺ ions drive the formation of Turing-type Ag₂Se patterns on the surface of CoSe₂ nanobelts.

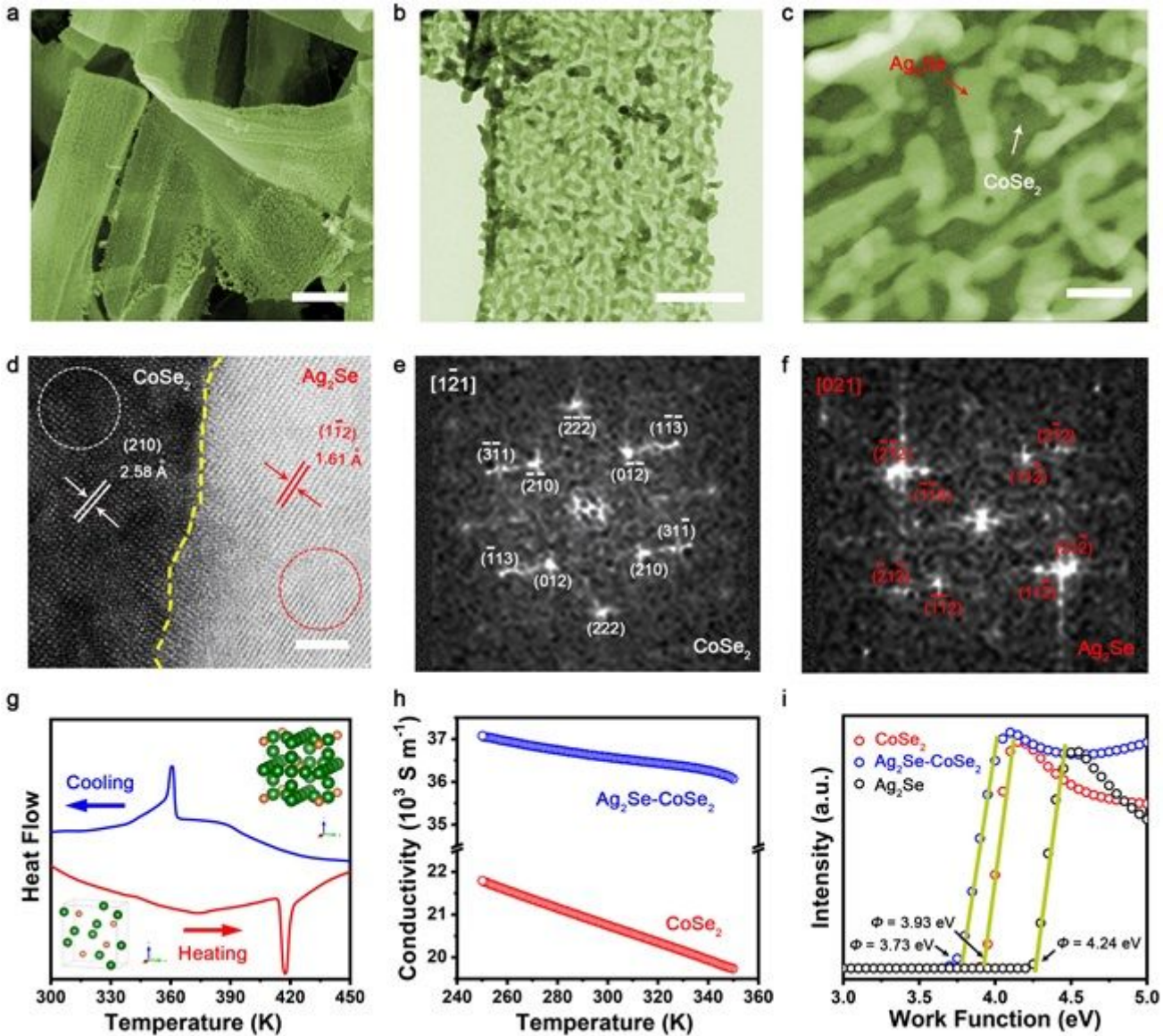


Figure 2

Physical characterization of Turing-type $\text{Ag}_2\text{Se-CoSe}_2$. a-c, SEM (a), TEM (b), and STEM (c) images of the $\text{Ag}_2\text{Se-CoSe}_2$. Scale bars, 400 nm (a), 250 nm (b), 50 nm (c). d, Atomic-resolution HAADF-STEM image showing the interface of $\text{Ag}_2\text{Se-CoSe}_2$. Scale bar, 2 nm. e, f, FFT patterns of CoSe_2 (e) and Ag_2Se area (f), which taken from the regions marked by the dashed white and red circles, respectively. g, DSC thermogram of $\text{Ag}_2\text{Se-CoSe}_2$. Insets show the model of the cubic (top) and orthorhombic (down) Ag_2Se . h, Temperature-dependent electrical conductivity for CoSe_2 and $\text{Ag}_2\text{Se-CoSe}_2$, respectively. i, UPS spectra of the CoSe_2 , Ag_2Se and $\text{Ag}_2\text{Se-CoSe}_2$.

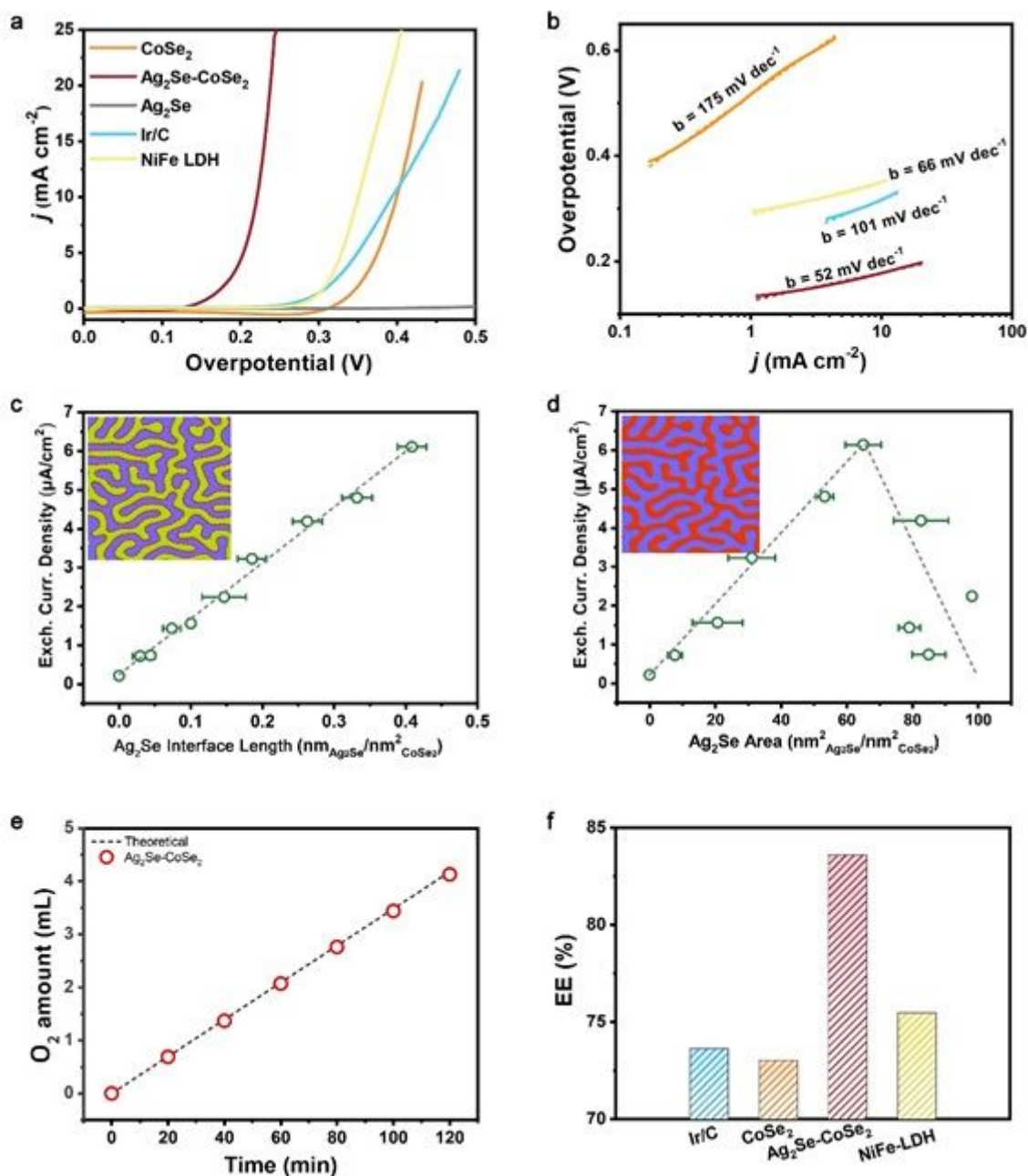


Figure 3

Electrocatalytic OER Performances of Ag₂Se-CoSe₂. a, OER polarization curves of different studied catalysts. Catalyst loading: 0.2 mg cm⁻². Sweep rate: 2 mV s⁻¹. b, Tafel plots of different catalysts derived from a. c, d, Exchange current density versus Ag₂Se-CoSe₂ interface length (c) and Ag₂Se area coverage (d). Insets in c and d schematically represent the Ag₂Se-CoSe₂ interface (red dotted line) and Ag₂Se area (red coverage), respectively. The exchange current density exhibits a linear dependence on the Ag₂Se-CoSe₂ interface length and a volcano-shaped dependence on Ag₂Se area coverage. Exchange current densities are extracted from the Tafel plot (Supplementary Fig. 20). The Ag₂Se-CoSe₂ interface length and Ag₂Se area coverage were calculated by using Digital Micrograph analysis (Supplementary Figs. 21 and 22). Error bars are based on the standard deviation of three independent measurements. e, GC-measured O₂ amounts at different time intervals, which agree well with the theoretical values,

suggesting a device Faradaic efficiency of $\sim 100\%$. f, Comparison of the anodic energy efficiency of the Ir/C, CoSe₂, Ag₂Se-CoSe₂ and NiFe-LDH catalysts.

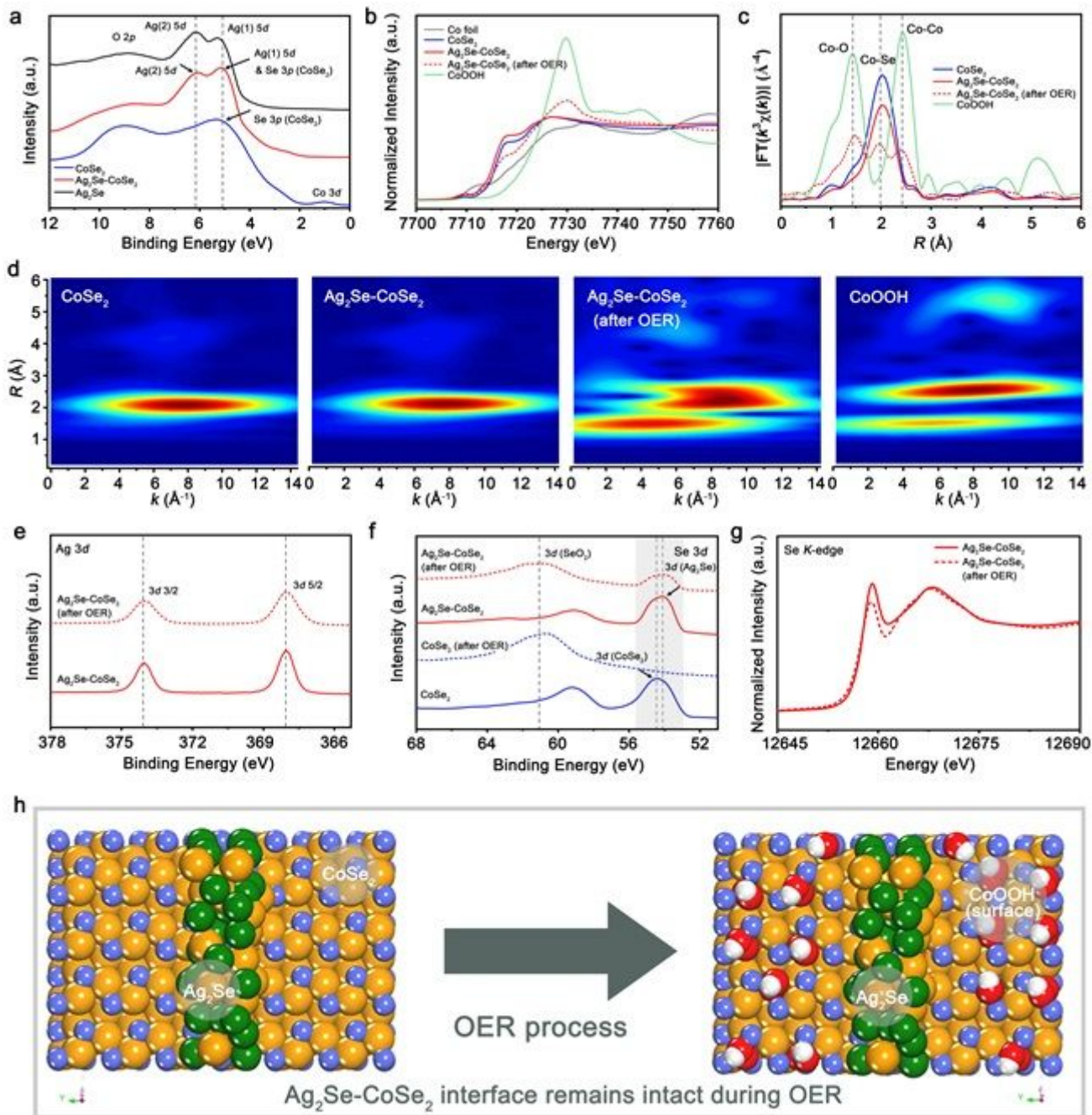


Figure 4

Spectroscopic studies of Ag₂Se-CoSe₂ before and after OER. a, Valence band edge spectra of Ag₂Se, Ag₂Se-CoSe₂ and CoSe₂ catalysts, respectively. b, c, Co K-edge XANES and corresponding k₃-weighted Fourier transforms spectra for CoSe₂, CoOOH, Ag₂Se-CoSe₂ before and after OER, respectively. d, Corresponding wavelet transforms of k₃-weighted EXAFS spectra of Co K-edge. e, Ag 3d XPS spectra of Ag₂Se-CoSe₂ before and after OER test. f, XPS spectra of CoSe₂ and Ag₂Se-CoSe₂ before and after OER in Se 3d region. g, Se K-edge XANES for Ag₂Se-CoSe₂ before and after OER. h, Schematic of the unique

surface-reconstruction feature of the Ag₂Se-CoSe₂ catalyst, showing that the Ag₂Se-CoSe₂ interface is robust without surface self-reconstruction during OER process.

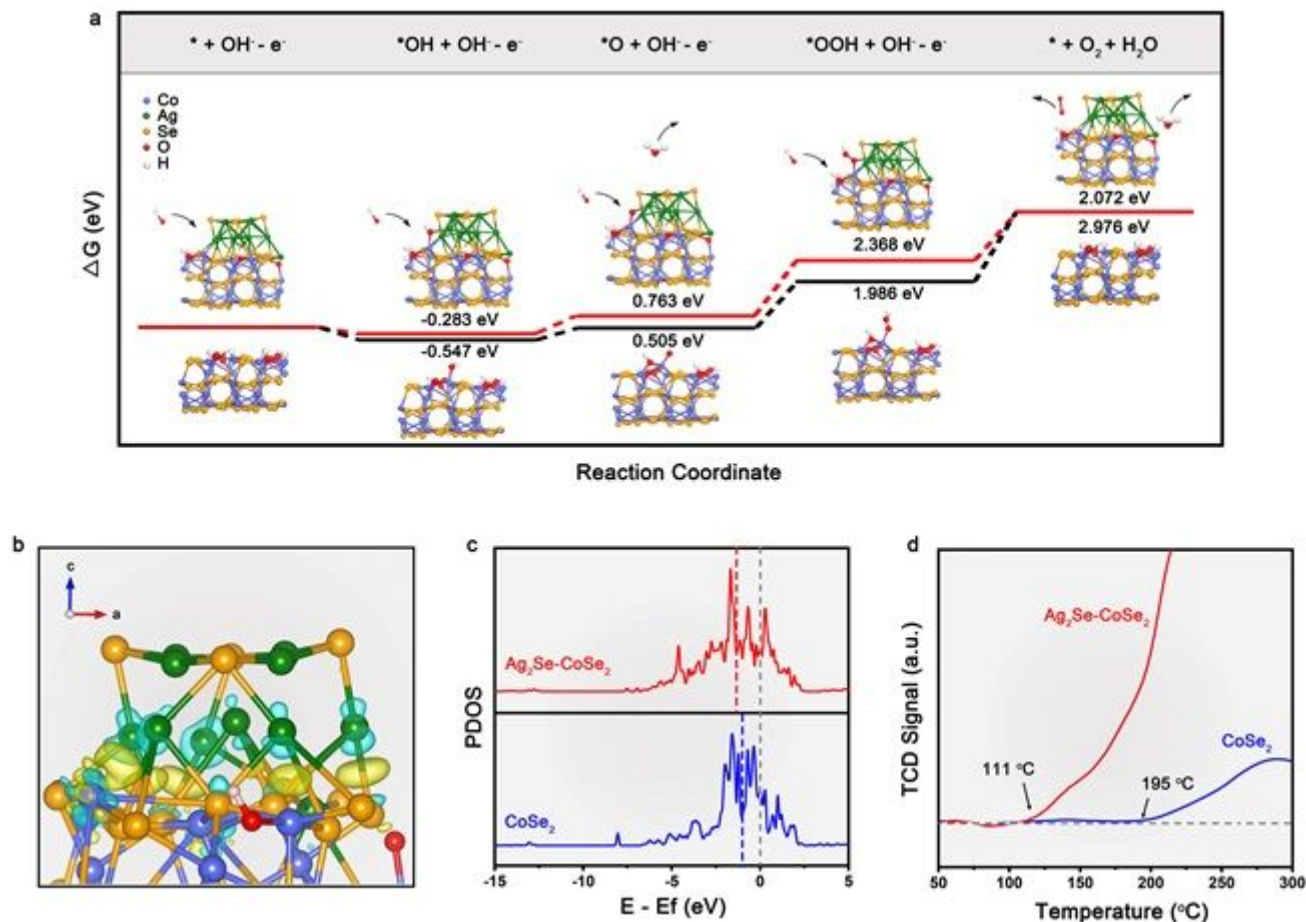


Figure 5

DFT calculations and enhancement mechanism. a, Gibbs free energy change diagrams of the OER process on the CoSe₂ (black line) and Ag₂Se-CoSe₂ (red line) surface models (both terminated with OH groups). b, Three-dimensional electron density difference on the Ag₂Se-CoSe₂ interface. The cyan and yellow contours represent electron density depressions and accumulations, respectively. c, Calculated density of states (DOS) of CoSe₂ and Ag₂Se-CoSe₂ with the Fermi level aligned at 0 eV. Blue and red dashed line located at the d-band center of CoSe₂ and Ag₂Se-CoSe₂, respectively. d, Temperature-programmed O₂ desorption analyses for CoSe₂ and Ag₂Se-CoSe₂ catalysts, respectively.

Supplementary Files

This is a list of supplementary files associated with this preprint. Click to download.

- [SITuringtypecatalyst.pdf](#)
- [Formulas.pdf](#)